Supplementary Information (SI) for Dalton Transactions.
This journal is © The Royal Society of Chemistry 2025

Supporting Information

Effects of Labile Ligands and Substituents in Nickel Enolate Catalysts on Ethylene/Acrylate Copolymerization Activity: A DFT Study

Ying Wang,[1,2] Xiaowei Xu,[1] Yi Luo,[1] Sicong Liu,[1] Zhuozheng Wang,[1] Hao Li,[1] Fan Yang,[2,*] Xingxun Li[2,*] Weisheng Yang[1,*]

[1]*PetroChina Petrochemical Research Institute, Beijing 102206, China*

[2]*State Key Laboratory of Heavy Oil Processing, China University of Petroleum-Beijing, Beijing 102249, China*

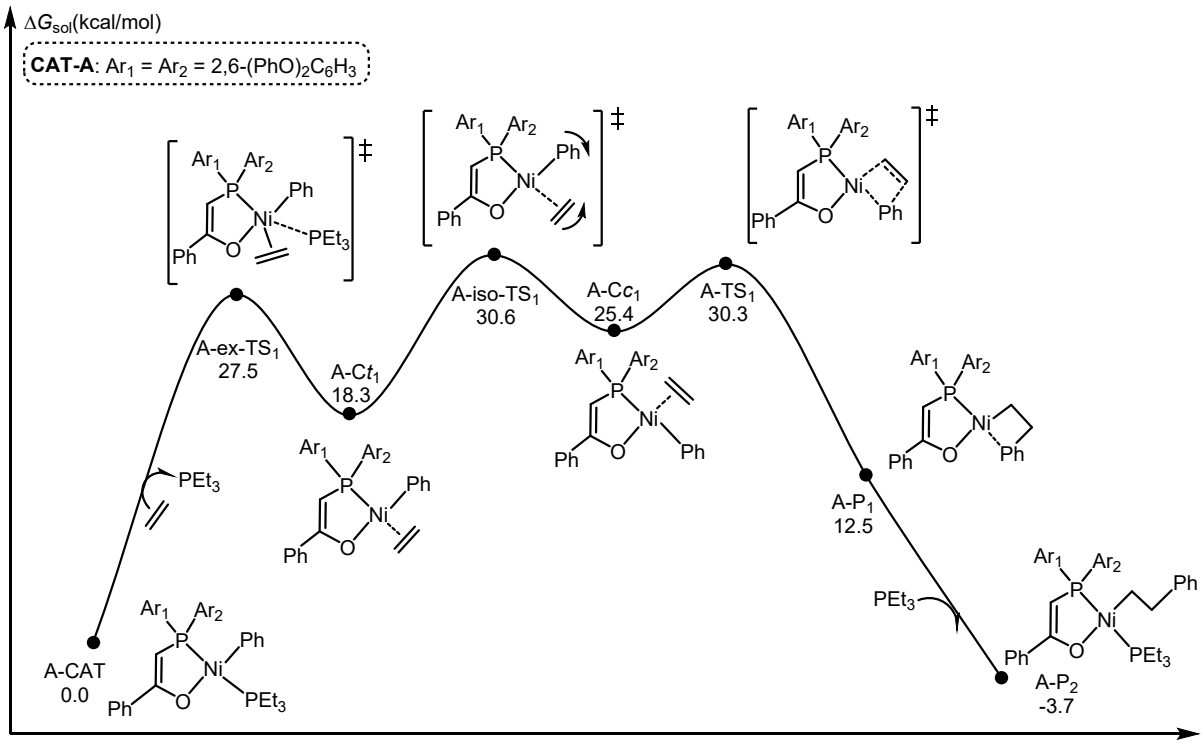

Figure S1. Energy Profile of Ligand Exchange and Subsequent *trans/cis* Isomerization in Catalyst **A**. The energies are relative to corresponding reactants.

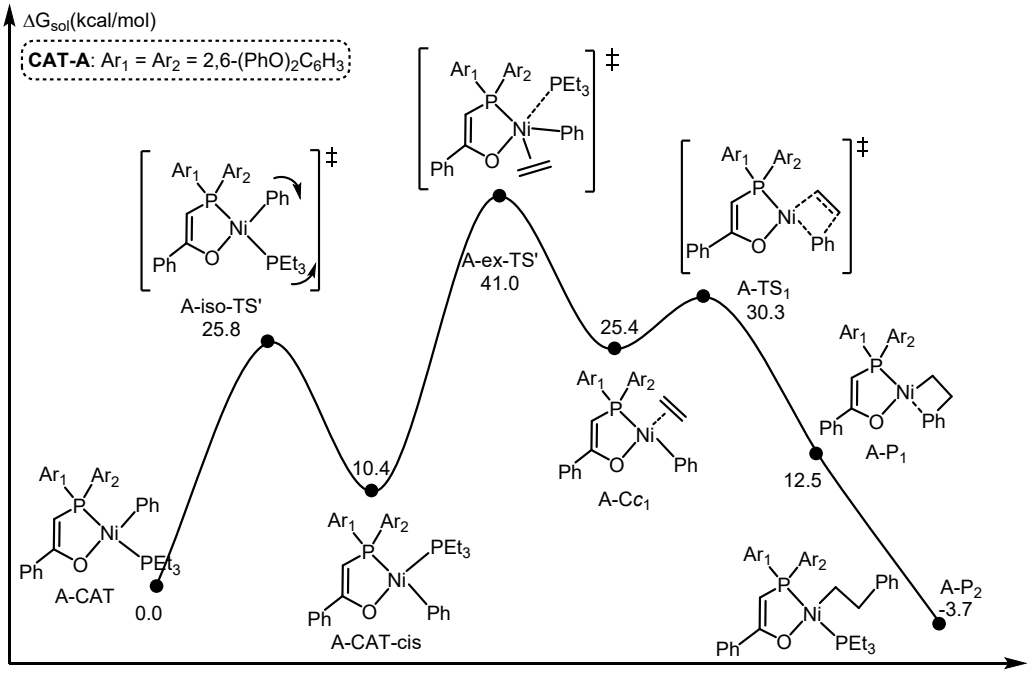

Figure S2. Energy profile of *trans/cis* Isomerization and Subsequent Ligand Exchange in Catalyst **A**. The energies are relative to corresponding reactants.

To elucidate the complete reaction pathway during chain initiation, we evaluated two distinct migratory-insertion pathways for catalyst **A**. In Path 1 (Figure S1), ligand exchange precedes *trans/cis* isomerization, whereas in Path 2 (Figure S2), the isomerization step occurs first. Analysis of the energy barriers reveals that the ligand exchange step in Path 2 is kinetically disfavored, exhibiting a substantially higher barrier of 41.0 kcal mol^{-1}. Consequently, the migratory-insertion process proceeds predominantly via the sequence outlined in Path 1 (Figure S1). Based on this mechanistic framework, the complete chain initiation pathway for catalyst **B** was then investigated. The energetic comparison of the chain initiation stages between the two catalysts is presented in Figure 2.

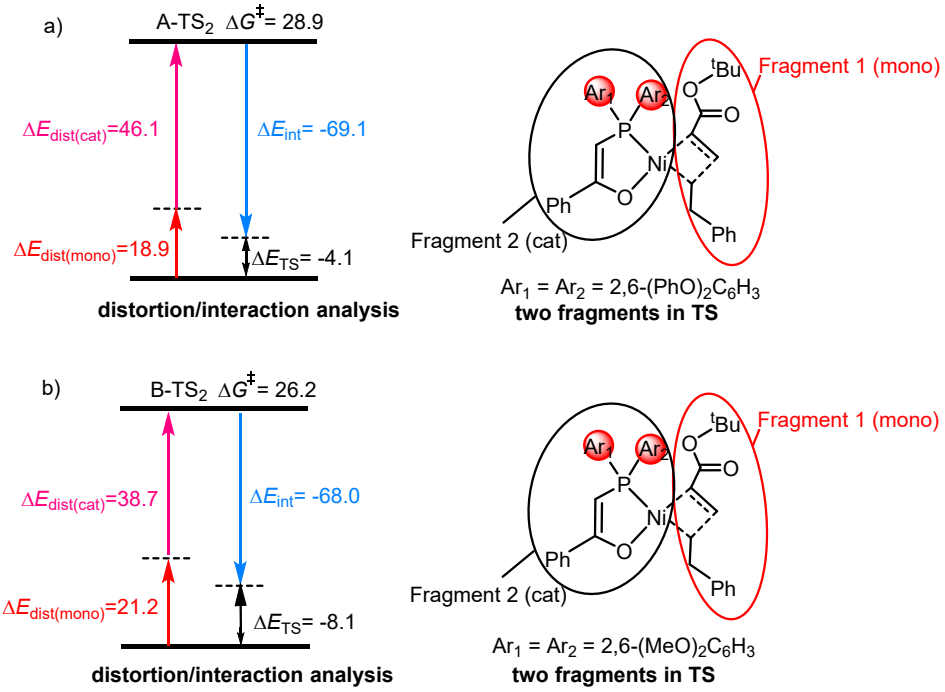

Figure S3. The distortion/interaction analysis (energy in kcal mol^{-1}) and the optimized structures of (a) **A-TS$_2$** and (b) **B-TS$_2$**.

As shown in Figure S3, the distortion/interaction analysis of the tBA insertion process is presented. The distortion energy of the catalyst fragment in the transition state is labeled in pink ($\Delta E_{dist(cat)}$), while the distortion energy of the monomer fragment is marked in red ($\Delta E_{dist(mono)}$). The calculation results indicate that in **A-TS$_2$**, the distortion energy of the monomer is 18.9 kcal·mol^{-1}, and that of the catalyst fragment is 46.1 kcal·mol^{-1}, resulting in a total distortion energy of 65.0 kcal·mol^{-1}.

In contrast, for **B-TS$_2$**, the distortion energies of the monomer and catalyst fragment are 21.2 kcal·mol^{-1} and 38.7 kcal·mol^{-1}, respectively, with a total deformation energy of 59.9 kcal·mol^{-1}. Comparatively, the total distortion energy of **A-TS$_2$** is significantly higher than that of **B-TS$_2$** (65.0 *vs.* 59.9 kcal·mol^{-1}). Although the interaction between the monomer unit and the metal catalyst is stronger in **A-TS$_2$** (with ΔE_{int} values of – 69.1 and – 68.0 kcal·mol^{-1} for **A-TS$_2$** and **B-TS$_2$**, respectively), it is still insufficient to compensate for the energy loss caused by the deformation energy. This is primarily due to the significant geometric distortion of **A-CAT** during the reaction process under the influence of steric hindrance, making distortion energy the dominant factor. As a result, catalyst **A** exhibits lower insertion efficiency during tBA insertion.

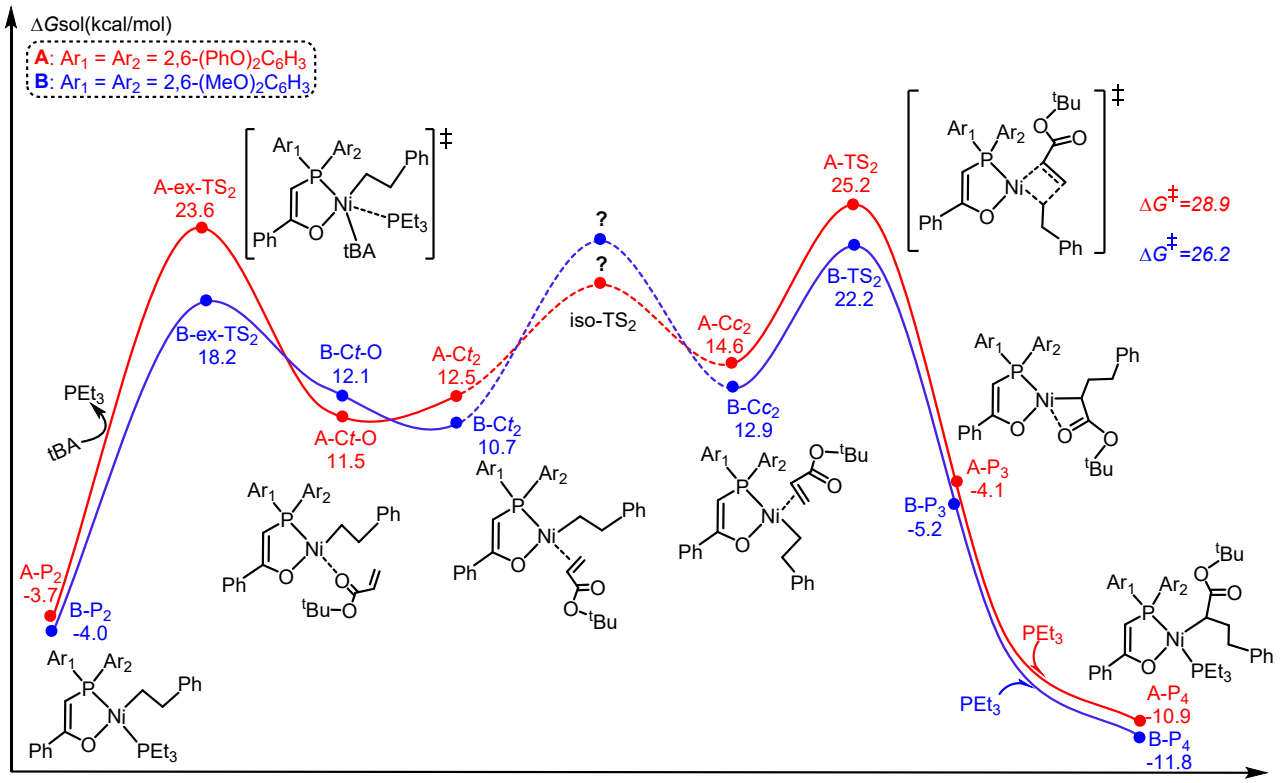

Figure S4. Energy profiles for tBA incorporation. The energies are relative to corresponding reactants.

Figure S4 presents the complete potential energy surfaces for the tert-butyl acrylate (tBA) insertion process catalyzed by catalysts **A** and **B**. The calculated barriers reveal that for catalyst **A**, the ligand exchange barrier is 27.3 kcal mol^{-1} and the tBA insertion barrier is 28.9 kcal mol^{-1}. In contrast,

for catalyst **B**, the ligand exchange barrier is significantly lower at 18.2 kcal mol^{-1}, which is also lower than its ethylene insertion barrier (26.2 kcal mol^{-1}). Regarding the *trans/cis* isomerization process, attempts to locate the isomerization transition state were fruitless. Given the substantial steric bulk of both the tBA molecule and the alkyl chains in the current system, it is not unexpected that locating such isomerization transition states within such a complex conformational space proved difficult.

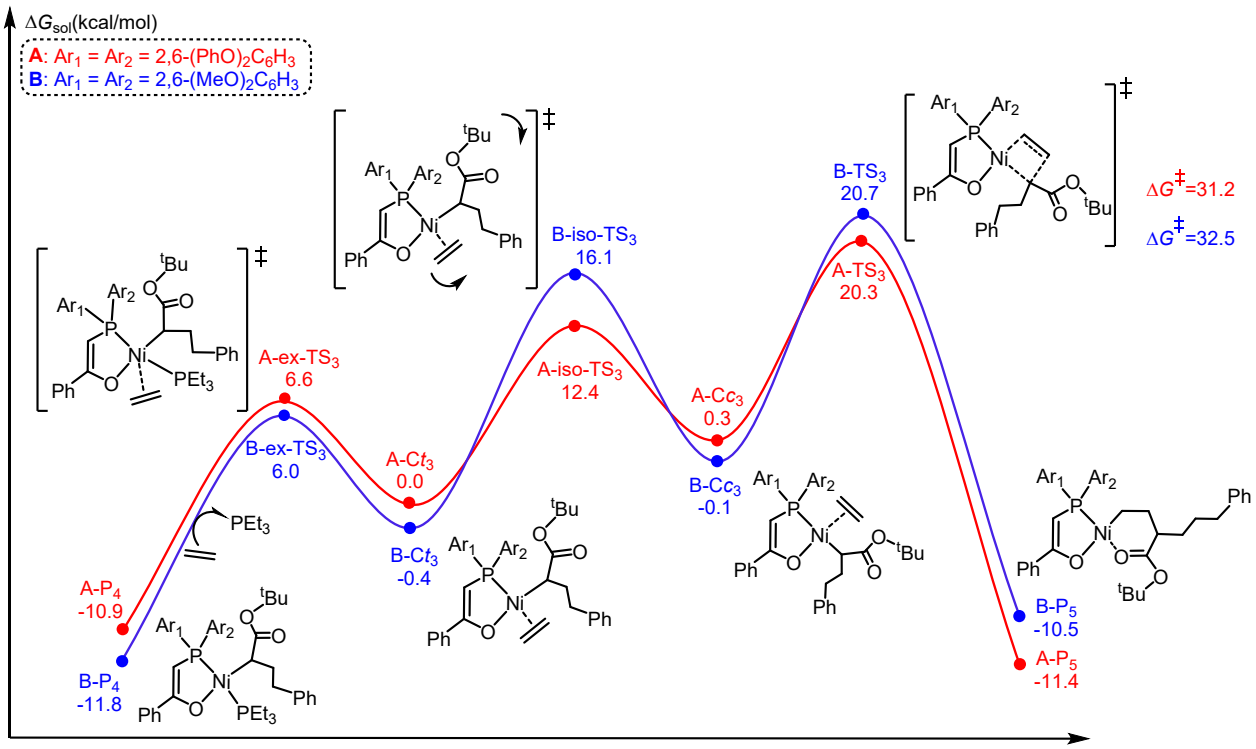

Figure S5. Energy profiles for ethylene insertion following tBA incorporation. The energies are relative to corresponding reactants.

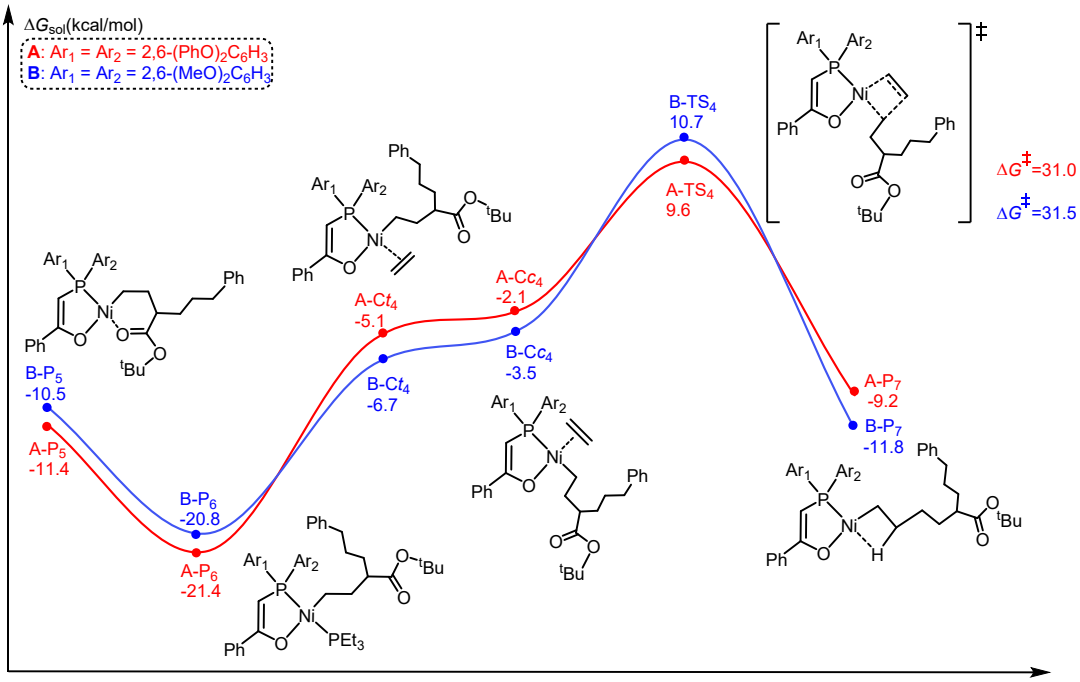

Figure S6. Energy profiles for ethylene insertion from intermediate $\mathbf{P_5}$. The energies are relative to corresponding reactants.

Table S1. A Comparison of Energy Barriers (kcal mol^{-1}) under Different Computational Protocol.

Ethylene insertion into the tBA pre-inserted chain-end[c,d]				
System and Protocol	**A-P$_4$** **(B-P$_4$)**	**A-TS$_3$** **(B-TS$_3$)**	**$\Delta G^{\ddagger}$(A)** **($\Delta G^{\ddagger}$(B))**	**$\Delta\Delta G^{\ddagger}$**
tpsstpss+d3bj[a]	-16.4 (-16.8)	15.6 (15.9)	32.0 (32.5)	0.5
M06+d3[b]	-23.0 (-22.7)	12.8 (13.8)	35.8 (36.6)	0.8
M06[b]	-16.4 (-17.1)	12.7 (13.7)	29.1 (30.8)	1.7
BP86[b]	5.3 (3.0)	17.9 (18.5)	12.6 (15.5)	2.9
WB97XD[b]	-18.9 (-20.2)	13.9 (14.3)	32.8 (34.5)	1.7

[a]For C, H, O, N, and P elements, using the 6-311G(d,p) basis set; for the Ni element, employing the SDD pseudopotential basis set.

[b]Apply the def2-TZVP basis set uniformly to all atoms in the entire system.

[c]The table includes only the key structural data calculated for the copolymerization energy barriers. [d]All single-point calculations were performed on the geometries optimized at the tpsstpss/6-31g(d) ∪ LanL2DZ level of theory.

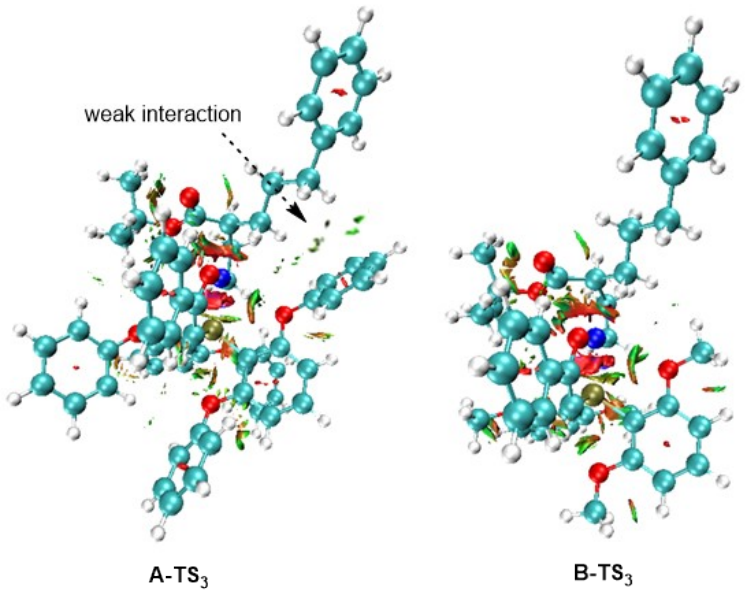

Figure S7. Noncovalent interaction (NCI) analysis for **A-TS$_3$** and **B-TS$_3$**.

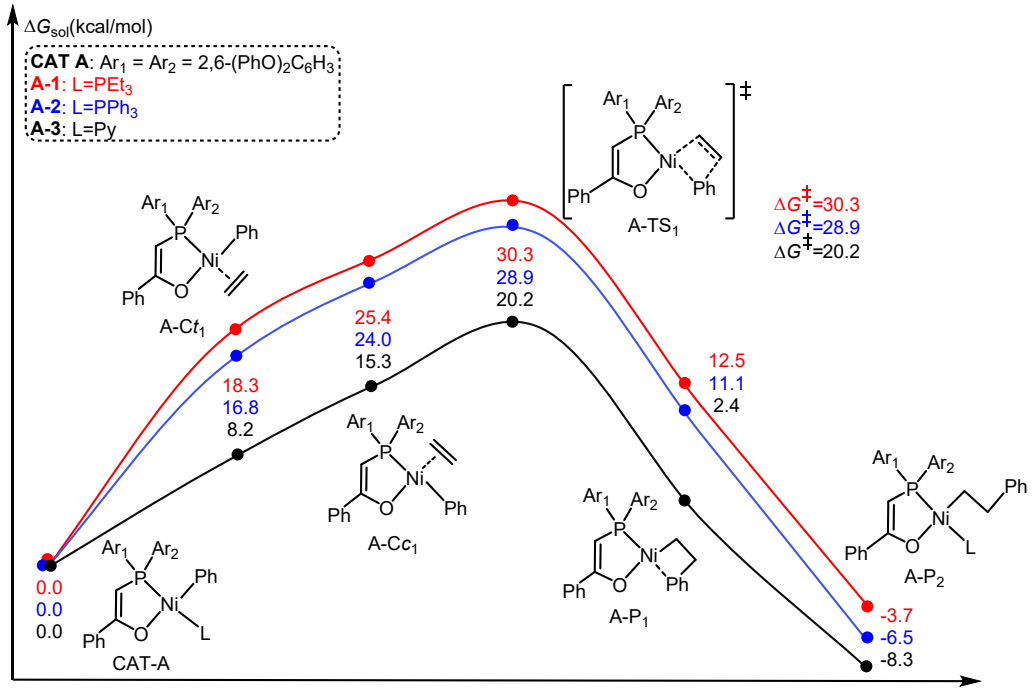

Figure S8. Energy profiles for chain initiation in **A** with three labile ligands. The energies are relative to corresponding reactants.

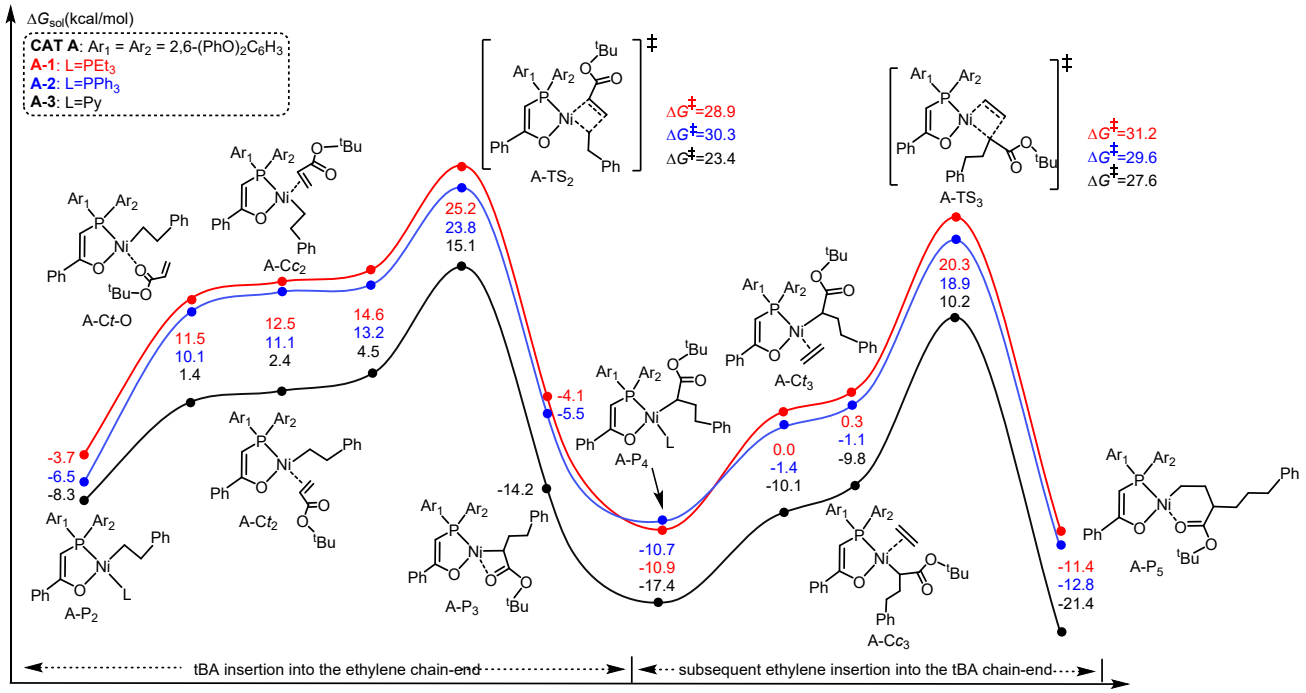

Figure S9. Energy profiles for chain propagation mediated by **A** with three labile ligands, including tBA insertion into the ethylene chain-end and subsequent ethylene insertion into the tBA chain-end. The energies are relative to corresponding reactants.

Figures S8 and S9 illustrate the differences in copolymerization activity of catalyst **A** with different labile ligands (L). When the ligand is pyridine (Py), catalyst **A** shows a chain initiation barrier of 20.2 kcal mol^{-1} and a rate-determining propagation barrier of 27.6 kcal mol^{-1}. This "fast initiation, slow propagation" profile corresponds to the highest activity observed for catalyst **A**. In contrast, with triethylphosphine (PEt_3) as the ligand, the stronger coordination ability of PEt_3 results in a "slow initiation, slow propagation" behavior. These computational trends are consistent with experimental observations, further validating the proposed mechanistic model.